Reduction of motion artefacts in on-board cone beam CT by warping of projection images

T E Marchant[1], G J Price[1], B J Matuszewski[2] and C J Moore[1].

[1]North Western Medical Physics, The Christie NHS Foundation Trust, Manchester, UK
[2]School of Computing Engineering and Physical Sciences, University of Central Lancashire, Preston, UK

Abstract
A local motion correction method for flat panel imager based cone beam (CB) CT by warping of projection images has been developed and tested. Markers within or on the surface of the patient are tracked and their mean 3D position is calculated. The 2D CB projection images are then warped before reconstruction to place each marker at the projection from its mean 3D position. The motion correction method was tested using simulated CB projection images of a deforming virtual phantom, real CBCT images of a moving breast phantom and clinical CBCT images of breast and pancreas radiotherapy patients. In phantom studies, the method was shown to greatly reduce motion artefacts in the locality of the radiotherapy target and allowed the true surface shape to be accurately recovered. The breast phantom, motion compensated surface was within 1mm of the true surface shape for 90% of surface points and greater than 2mm from the true surface at only 2% of points. Clinical CBCT images showed improved image quality in the locality of the radiotherapy target after motion correction.

1   Introduction

Motion artefacts in cone beam CT (CBCT) occur due to movement of the patient during scan acquisition leading to inconsistent data for 3D reconstruction. This is a particular problem for flat panel imager based cone beam CT systems used in image guided radiotherapy, where the scanner rotation speed is limited, leading to acquisition times of 1-2 minutes. Physiological motions such as breathing or internal gas movements lead to anisotropic disturbance, with consequential blurring and streak artefacts in the reconstructed CBCT images [1, 2]. These impede the accurate local delineation of tumours, organs and body surface, which is important for image guided radiation therapy (IGRT). In IGRT, it is common to acquire a CBCT image immediately prior to treatment delivery for the purpose of verifying that the patient and the relevant internal structures are positioned as intended. If motion artefacts can be removed, making the position of these important objects easier to identify, then the value of the images for geometric verification in radiotherapy may be greatly enhanced.

A number of methods have been used to reduce the severity of motion artefacts in CBCT. Elimination of the motion at source, for example through use of breath hold during acquisition [3] is effective but not applicable in all situations. Sorting of projections into different breathing phases to produce respiratory correlated CBCT reconstructions has also been reported [4-6]. This requires acquisition of additional projections (with correspondingly increased patient dose), and is only applicable to periodic motions such as breathing.

Methods to compensate motion effects during the reconstruction can be applied in 3D, where the attenuation distribution to be reconstructed is treated as a function of time, and the motion path of each voxel is derived from a prior motion model [7-10]. However, a prior motion model is not always available or may be inaccurate.

Alternatively, corrections can be applied to the projection data before back projection. Lu and Mackie [11] described a motion correction for fan-beam CT, tracking in-plane motion of nodal points in the sinogram and using this to derive patient motion according to a simple model. The sinogram data was then adjusted to correct for this motion.

A method of shifting CBCT projection images based on the position of markers attached to a moving rigid phantom has been shown to reduce motion artefacts [12]. Perrenot et al. [13] and Schäfer et al. [14] used two markers attached to a coronary stent to define an affine transformation of each projection image, in order to match the marker positions to the forward projection of their position at a chosen reference time. A more complex projection-based motion correction by warping projection images was described by Hansis et al. [15]. Projection images from 3D coronary angiography were warped to reduce discrepancies between measured vessel positions and forward projected vessel positions from an initial ECG gated reconstruction.

These 2D corrections, applied in the projection image domain, are more approximate in nature than the 3D methods. Overlying structures in a projection image, which do not have identical motions, cannot both be corrected by manipulating data in the projection domain. However the corrections can be valid in a local region, or where motion may be considered to be approximately rigid. Correction of motion artefacts in a local region can be particularly useful for CBCT images used for target position verification in radiotherapy. Here, sufficient image quality in the region of the radiotherapy target is necessary to allow assessment of its position in relation to the applied radiation beams. Corrections in the projection domain can be simpler to apply than full 3D corrections and do not require a prior motion model.

In this paper we describe a motion compensation method for CBCT using a limited number of radio-opaque markers tracked in the projection data. This allows the mean 3D position of each marker to be determined [16]. Projection images are then warped to place each marker at the forward projected mean position for that marker. The method is demonstrated for both markers placed on the surface of the patient and implanted fiducial markers within the patient, as are widely used in radiotherapy [17, 18].

We apply the proposed motion compensation method to images from a wide angle CBCT scanner integrated with a radiotherapy linear accelerator. Improvements in image quality are demonstrated for both phantom and clinical images.

2 Materials and Methods

2.1 Projection image warping

A set of markers is identified that are visible in all of the CBCT projection images. These may be artificially added markers either on the surface or within the object, or natural features of the object itself. The marker positions are then identified on each projection image, yielding a set of image coordinates as a function of gantry angle for each marker, $(u_{i,j}, v_{i,j})$ where $u_{i,j}$ and $v_{i,j}$ are the u and v positions respectively of the ith marker on the orthogonal major axes of the jth rectangular projection image. Axis v is parallel with the axis of rotation of the CBCT scanner, which coincides with the inferior-superior direction of a patient lying head first into the scanner. Since the gantry angle, θ_j, of each projection image is known, the marker positions can be fitted to functions describing the image coordinate of a projected static 3D point as a function of gantry angle [16]. The projection image coordinates, $u(\theta)$ and $v(\theta)$, of the point (x,y,z) at gantry angle θ are given by

$$u(\theta) = \frac{(x\sin\theta + y\cos\theta) \times SDD}{SAD - (x\cos\theta - y\sin\theta)} \qquad (1)$$

$$v(\theta) = \frac{z \times SDD}{SAD - (x\cos\theta - y\sin\theta)}, \qquad (2)$$

for a CBCT system with source to detector distance SDD and source to axis of rotation distance SAD.

This fit yields the mean 3D position of each marker, $(\bar{x}_i, \bar{y}_i, \bar{z}_i)$, and the corresponding coordinates of the projection of that mean position in each projection image, $(\bar{u}_{i,j}, \bar{v}_{i,j})$.

Each projection image is then warped using the identified marker positions, $(u_{i,j}, v_{i,j})$, as control (tie) points in the input image and the projected mean positions as the corresponding control points in the warped image. The corners of each projection image were used as additional tie points with assumed zero motion. The images were warped smoothly using thin-plate spline interpolation [19]. Image processing was done using IDL (v6.3, ITT Visual Information Solutions, Boulder, USA). After warping, the image of each marker lies at the forward projection of its measured mean position. The warped projection images are then used as input for CBCT reconstruction. Figure 1 shows schematically a projection image with 6 markers before and after warping. The crosses indicate the projected mean positions of each marker, and the grid

is superimposed, for illustration purposes only, to show the smoothly interpolated warp field applied to the image.
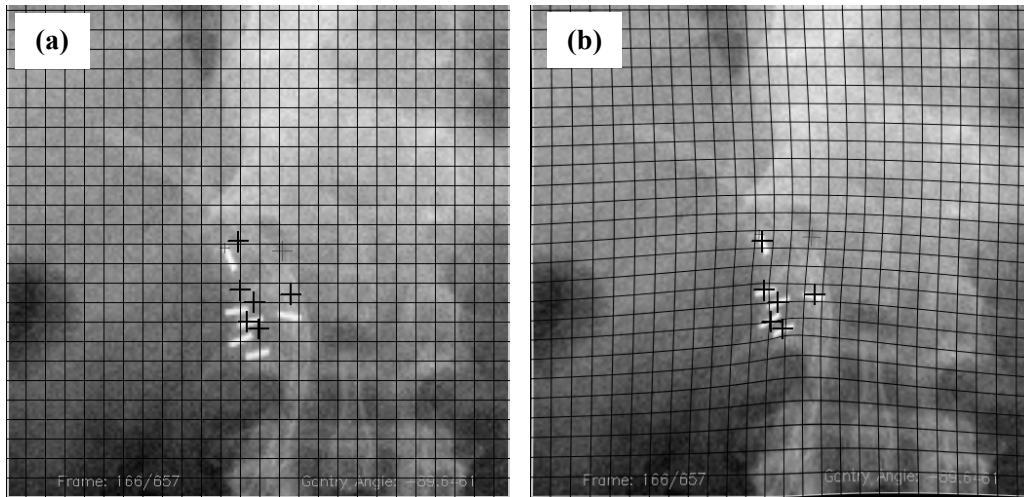

Figure 1: Schematic projection image (a) before and (b) after warping to place marker seeds at their projected mean position (dark crosses). Superimposed grid indicates smoothly interpolated warp field.

2.2 Image data

CBCT images were acquired with Elekta Synergy (XVI 3.5, Elekta, Crawley, UK). Projection images were acquired using a 512x512 sampling resolution (pixel size 0.5 mm, scaled to the isocentre). Breast phantom and patient images were acquired using a small field of view (imaging panel centred) protocol with 350 projection images evenly spaced over 200° with technique factors of 120kV, 16mA, 16ms per frame (scan dose 3.5mGy). Clinical pancreas images were acquired using a medium field of view (panel offset in u direction) protocol with 650 projection images evenly spaced over 360° and technique factors of 120kV, 10mA, 40ms per frame (scan dose 8.6mGy). CBCT images were reconstructed by a Feldkamp Davis Kress (FDK) filtered back projection algorithm [20] using a commercial software package (COBRA v5, Exxim, Pleasanton, USA), with 1mm voxel size in all directions.

2.3 Breast phantom

Images of a realistically shaped breast phantom were used to test the proposed motion correction method. The breast phantom was constructed using a rapid prototyping system that can produce a smooth, continuous outer shell supported by an underlying honeycomb structure. The breast phantom was placed onto a motorised, tilting platform to simulate periodic motion of the phantom during image acquisition (shown in figure 2a). Three spherical glass marker beads of 4mm diameter were placed onto the surface of the phantom, which could be tracked in the CBCT projection images. CBCT images were acquired of the static phantom and with the phantom moving with period of approximately 4 seconds and maximum amplitude of 15mm at the inferior edge of the phantom. The amplitude used here is larger than typically observed patient motion in breast radiotherapy [21], hence motion artefacts are expected be more severe than those observed in typical patient images.

The marker positions were identified in each 2D projection image of the moving phantom and used to warp the projections, as described in section 2.1, before reconstruction. The moving phantom 3D reconstructed images with and without motion compensation were compared. The

motion compensated moving phantom reconstruction was also compared to that of the static phantom. The two images were co-registered in 3D and the phantom surface shapes compared. This registration step removed differences in phantom position between the static image and the motion compensated image, which shows the mean phantom position.

A closest point metric was used to compare the shape of isosurfaces extracted from the two volumes. Iso-surfaces were created by thresholding at an appropriate value (approximately half way between the air value and the peak value in the phantom wall) and smoothed to remove noise using an erode-dilate procedure (element size 0.5mm). The two thresholded image surfaces were co-registered using the rigid body iterative closest point (ICP) algorithm [22] prior to using the final closest point distances as the error metric.
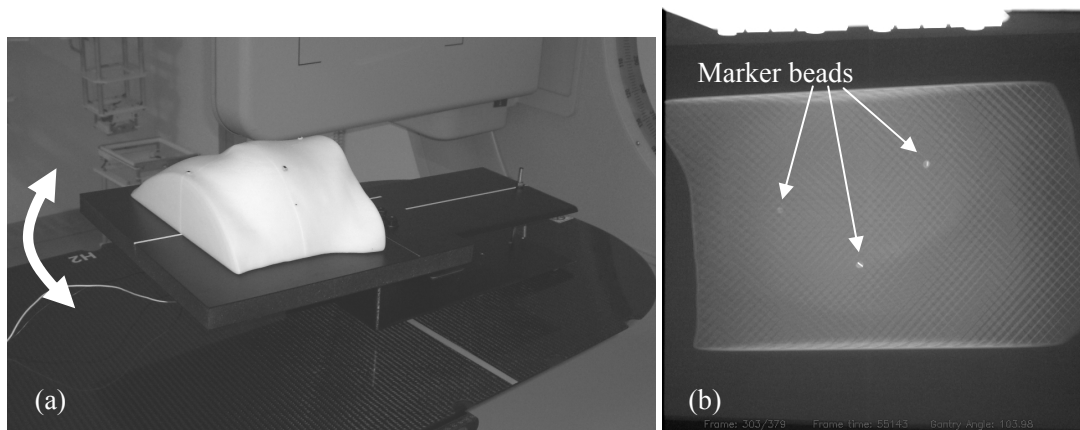

Figure 2. (a) Breast phantom and motorised, tilting platform. White arrow indicates motion direction of phantom. (b) Projection image from CBCT acquisition of moving breast phantom. The three marker beads placed on the surface are indicated.

2.4   Virtual phantom

Further testing of the proposed motion correction method was carried out using virtual phantoms, which allowed known deformations to be applied, as may be encountered in patient images. Two virtual phantoms were used. The first represents a low contrast ellipsoidal "tumour" moving within a static cylindrical "body" contour (example simulated projection images shown in Figure 3a and b and reconstructions in Figure 4a-c). Six fiducial markers are located within the tumour object, and the tumour is both translated along an elliptical path of peak-to-peak amplitude 4, 10 and 20 mm in the LR, AP and SI dimensions respectively, and deformed by stretching with a factor of 1.02, 1.05 and 1.10 in the LR, AP and SI directions respectively. The second virtual phantom represents a cylindrical patient outline moving with a stylised breathing motion consisting of a volume conserving warp with the posterior surface remaining fixed (indicated by dotted lines in Figure 5a). Five simulated fiducial markers are situated on the anterior surface of the object (locations indicated on the example simulated projection images shown in Figure 3c and d) and the position of the anterior surface moves by ±1.6 cm.

Projection images of the moving virtual phantoms were simulated using the *take* software (v2.1) [23]. Three images of each phantom were reconstructed: (i) static phantom, (ii) moving phantom and (iii) moving phantom with motion correction. Motions for both phantoms were applied with a simulated period of 4 seconds and so that the mean phantom position/shape was the same as the static phantom image. This allowed direct comparison of the motion corrected and static phantom images.
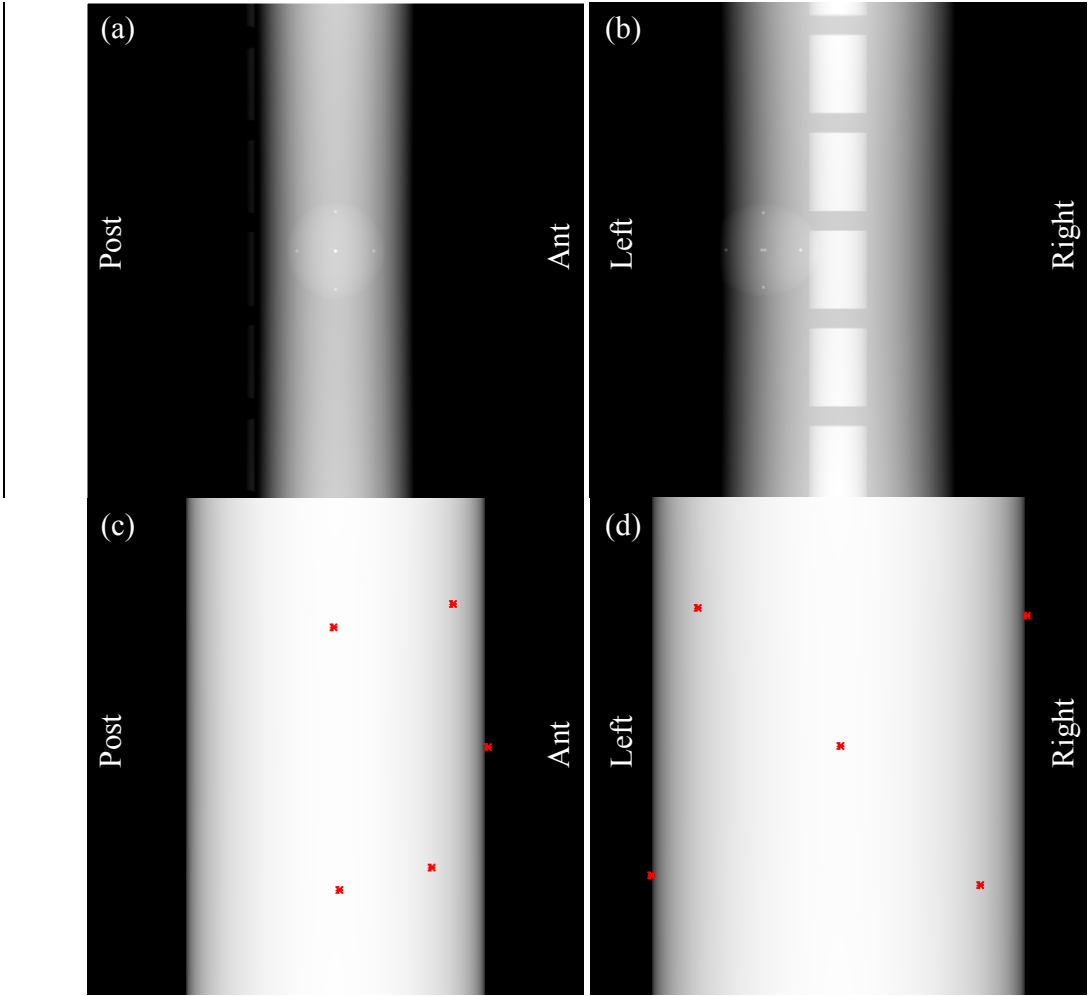
Figure 3: Simulated projection images showing virtual phantoms at their mean position. (a & b) Lateral and vertical projections through first virtual phantom. Note that the phantom surface is not visualised due to the narrow viewing window optimised to show low contrast object and markers. (c & d) Lateral and vertical projections through second virtual phantom. Red asterisks indicate locations of the surface markers (not visible directly due to large dynamic range of the image).
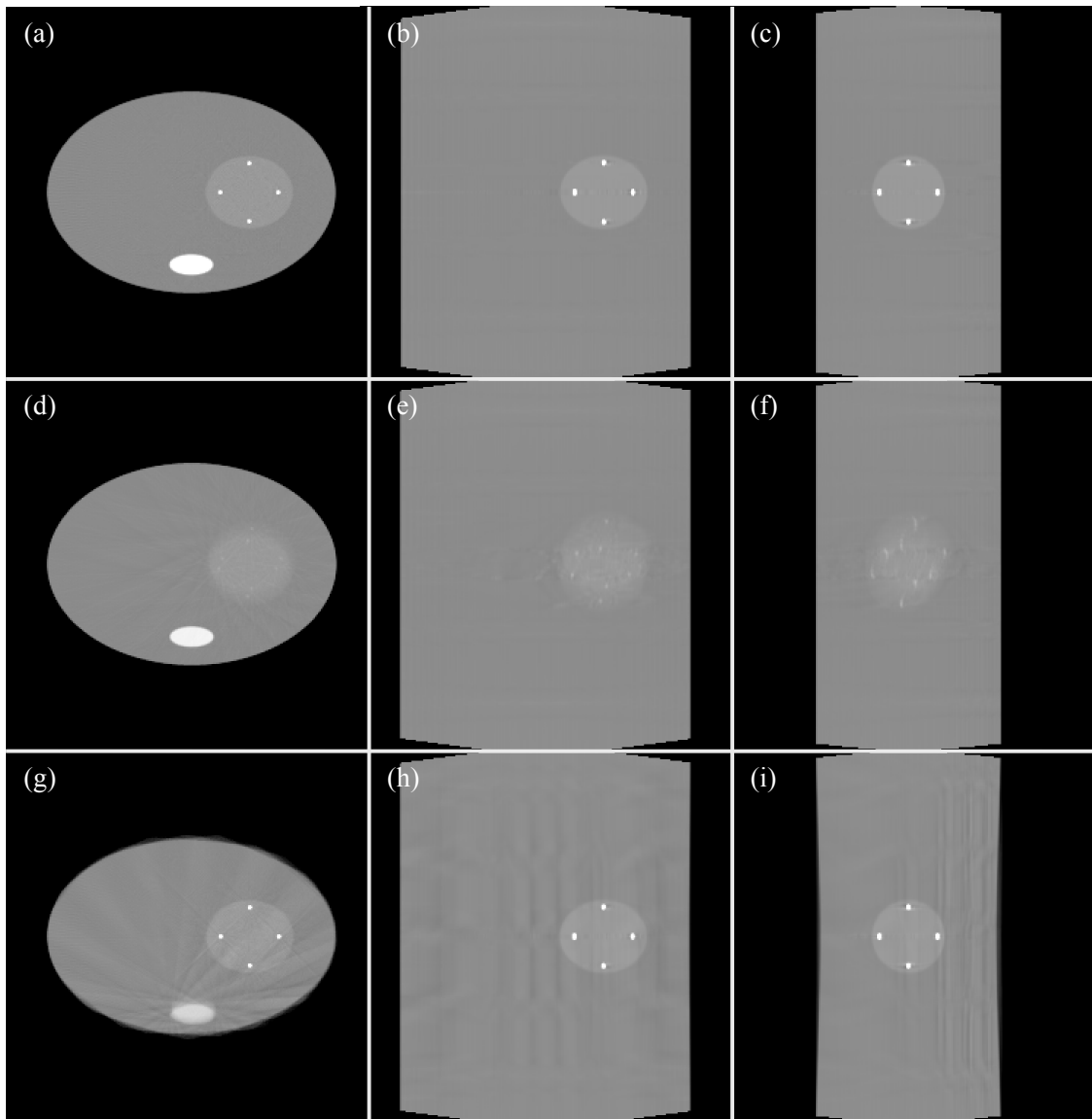
Figure 4: Virtual phantom reconstructed images. Top row (a-c) shows static phantom images. Middle row (d-f) shows moving phantom without motion compensation. Bottom row (g-i) shows moving phantom with motion correction applied. Left, middle and right columns show axial, coronal and sagittal slices respectively.
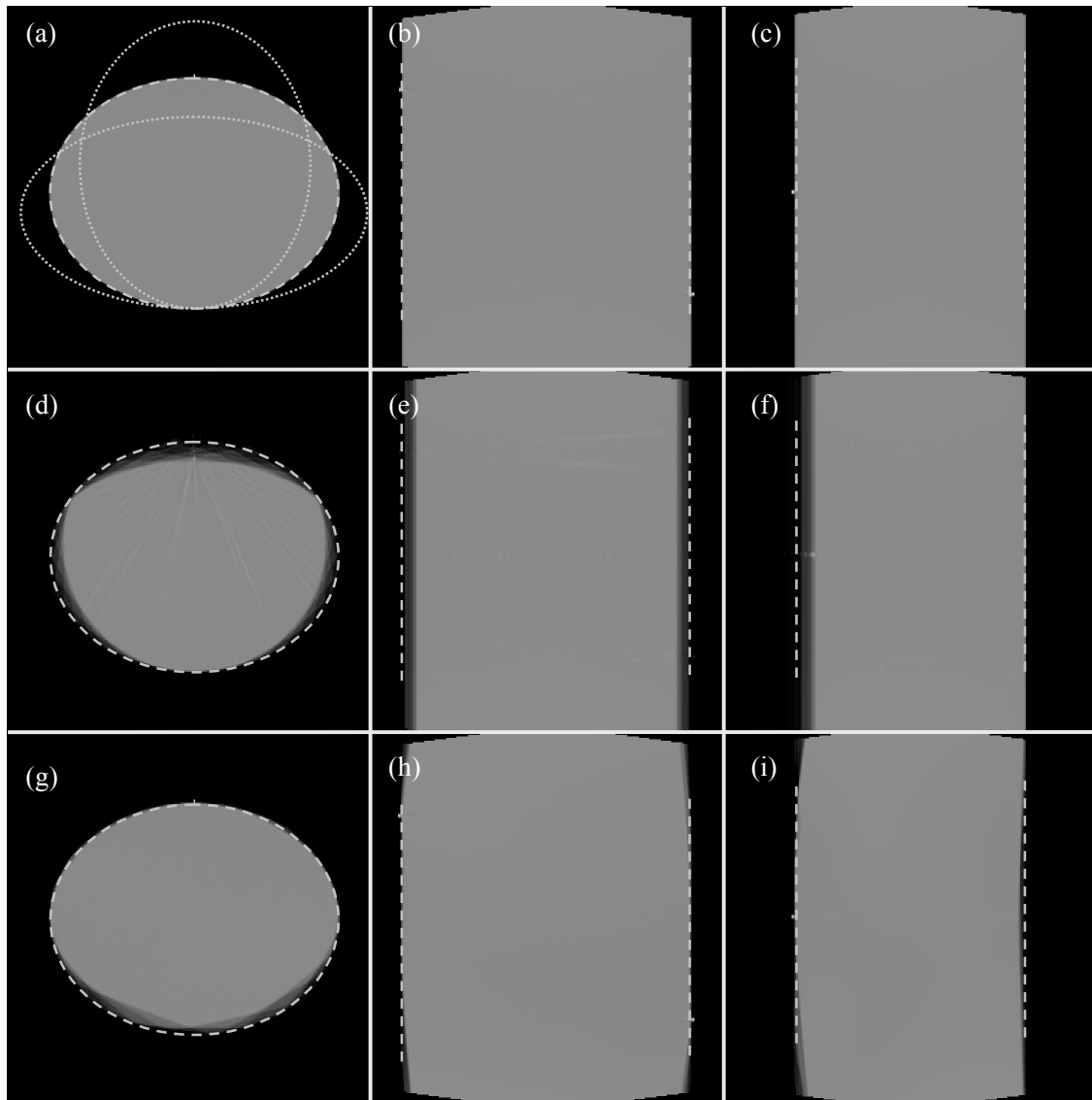
Figure 5: Virtual phantom reconstructed images. Top row (a-c) shows static phantom images. Middle row (d-f) shows moving phantom with no motion correction. Bottom row (g-i) shows moving phantom with motion correction applied. Left, middle and right columns show axial, coronal and sagittal slices respectively. Dashed lines indicate surface position of static phantom overlaid onto each image.

2.5   Patient images

The proposed motion correction method was also tested for effectiveness on clinical data using projections from CBCT images of a pancreatic cancer patient and a breast cancer patient. The pancreas patient had six gold seeds (1mm x 5mm) placed into the pancreas at surgery, a common procedure to improve tumour localisation for radiotherapy planning and delivery [24-26]. The breast patient had radiographic marker wires, as routinely used for radiotherapy treatment planning scans, placed onto the skin surface at the entry points of medial and lateral radiotherapy beams. Three positions on each marker wire could be tracked (each end plus the centre). The position of each marker was manually identified in each projection image, and used to warp the

projection images as described in section 2.1 before reconstruction. For the breast patient image, some of the markers could not be identified in all projection images due to low signal to noise ratio or overlying structures. This was the case of 11% of all possible marker identifications, although at least three points were identified for all projection images. Markers were omitted from the list of tie points for warping of projection images in which they could not be identified. The reconstructed images with and without motion compensation were compared.

3   Results

3.1   Breast phantom

Figure 2b shows a projection image from the moving breast phantom CBCT acquisition. The positions of the three surface marker beads are indicated. Figure 6 shows the projection image u and v coordinates as a function of gantry angle of one of the marker beads in the moving breast phantom image. The projected position of the determined mean marker position is also shown.
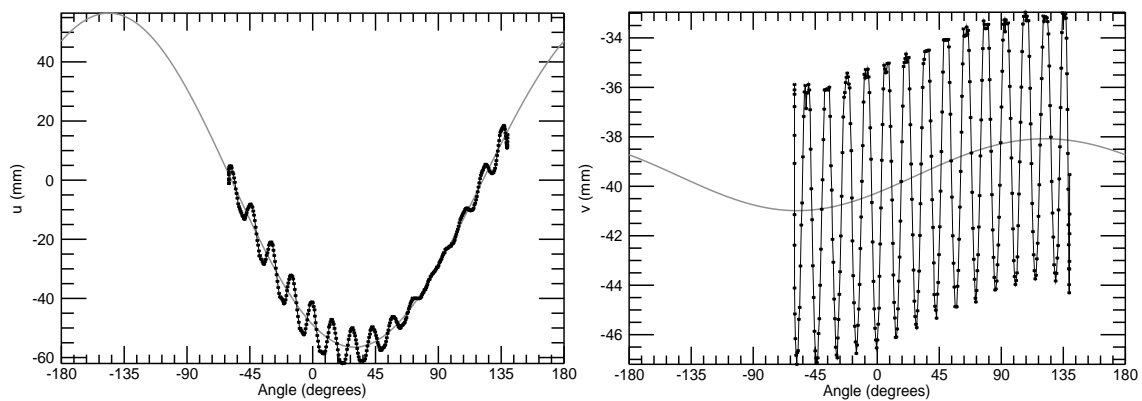

Figure 6: Projection image u and v coordinates of one marker bead in moving breast phantom image as a function of gantry angle. Points indicate observed positions, while the thick line indicates the projected position of the mean marker position.

Figure 7 shows CBCT reconstructed images of moving breast phantom with and without motion compensation. The quality of the images without motion compensation (figure 7a and figure 7c) is observed to be significantly poorer. Severe streak artefacts are present, which make it very difficult to even define the surface position. The quality of the motion compensated images (figure 7b and figure 7d) is observed to be much improved. The streak artefacts are much less severe and the surface position can now be defined.

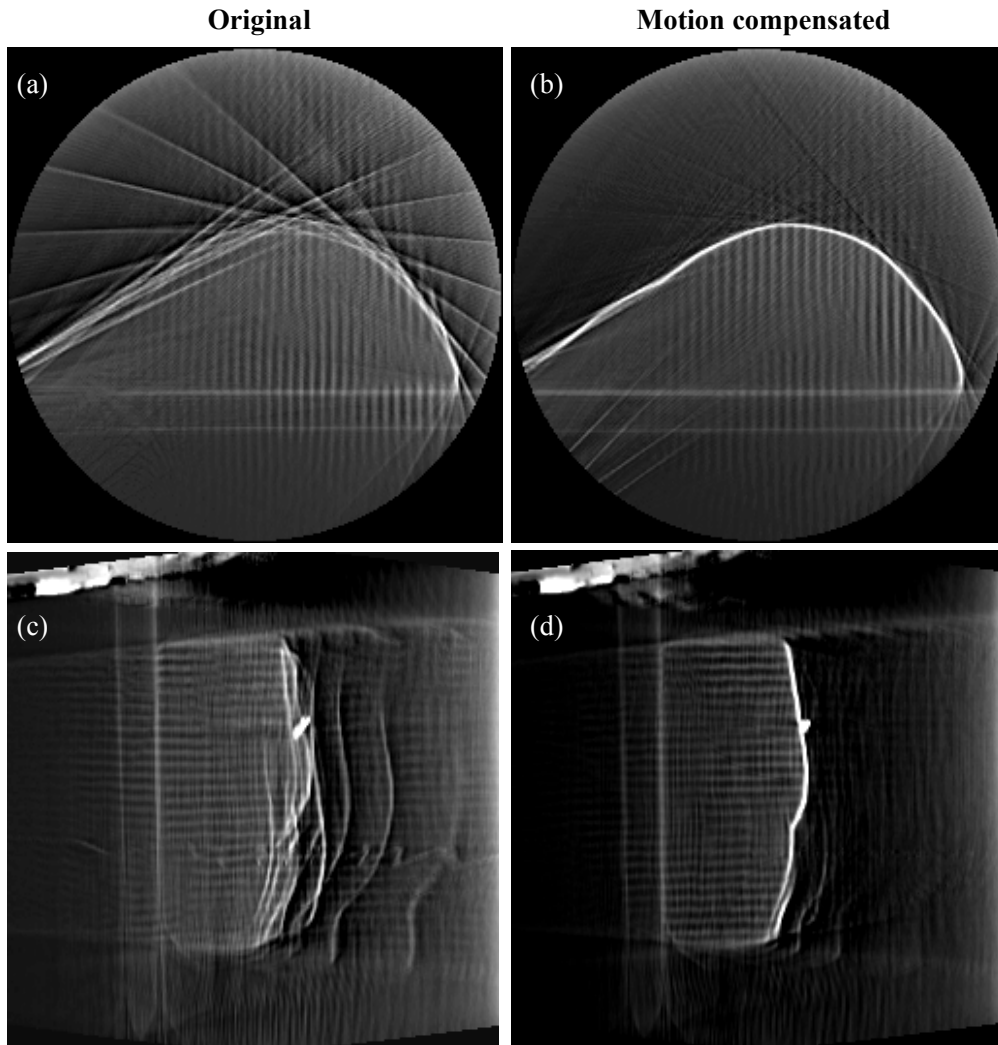**Original**   **Motion compensated**

Figure 7: CBCT reconstructed images of moving breast phantom with and without motion compensation. (a) transaxial slice without motion compensation, (b) transaxial slice with motion compensation, (c) sagittal slice without motion compensation (d) sagittal slice with motion compensation.

Figure 8 shows the breast phantom iso-surface extracted from the motion compensated CBCT image, with shading representing the distance between the surfaces segmented from the static phantom CBCT image and the dynamic phantom motion compensated CBCT image. The majority of the surface (90 %) has distance between the surfaces of less than 1 mm (indicated by white/light grey). Regions with distance between the surfaces of between 1 and 2 mm cover 8 % of the area (shown in green). Only a very few points (2 % of the surface) have distances greater than 2 mm (shown in red). The mean distance between the surfaces is 0.6 mm.

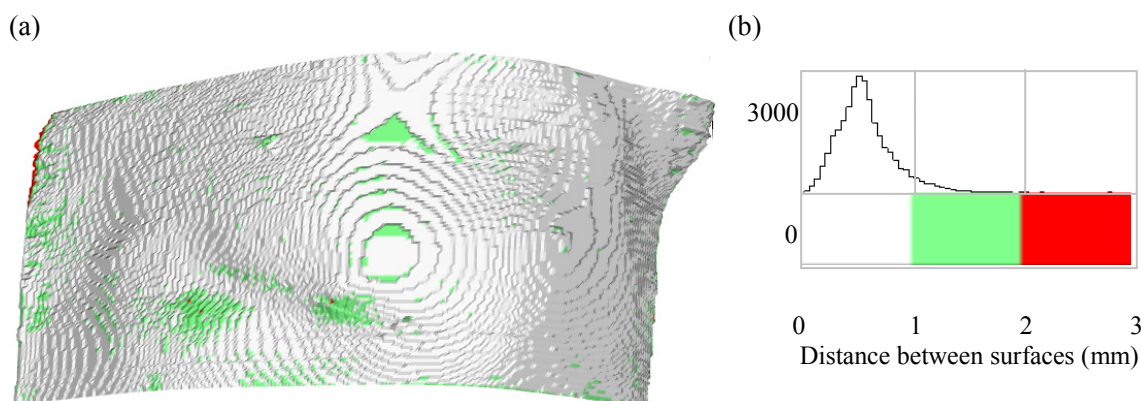(a)   (b)

Figure 8: (a) Surface map of breast phantom with colour shading indicating distances between the static phantom surface and the motion compensated dynamic phantom surface. White/grey indicates discrepancy less than 1mm, green indicates discrepancy between 1 and 2 mm, red indicates discrepancy greater than 2 mm. (b) Histogram showing number of surface points as a function of distance to agreement between the surfaces, and definition of colour shading of surface map.

3.2   Virtual phantom
Figure 4 shows reconstructed images from the virtual phantom with a moving and deforming "tumour" object within a static body outline. The top row shows slices from an image of the phantom with no motion. The second row shows the same slices from an image of the moving phantom. The edges of the tumour are severely blurred and the fiducial markers are no longer clearly visible. The bottom row shows the same slices with the proposed motion correction applied. The sharp edges of the tumour object have been restored at the correct mean position, and the fiducial markers are seen clearly. Some artefacts have been introduced in other areas of the image. In particular, there are streak artefacts emanating from the high-density objects representing the spine, and the surface of the phantom has been distorted in places.

Figure 5 shows reconstructed images from the second virtual phantom experiment with a cylindrical object subjected to a simulated breathing motion. The top row shows slices from an image of the phantom with no motion. The dashed grey lines indicate the surface position of the static phantom. The second row shows the same slices from an image of the moving phantom. The anterior and lateral surfaces of the phantom are very blurred and are not reconstructed in their correct mean position (as indicated by the dashed line). The bottom row shows the same slices with the proposed motion correction applied. The anterior and lateral surfaces of the phantom are now reconstructed much closer to their true mean position. It is noted that the posterior surface of the phantom appears distorted in the motion corrected image. This is because the tracked markers were only placed at anterior and lateral positions on the surface. Also the quality of the motion correction degrades superiorly and inferiorly (e.g. Figure 5h and i). This reflects the increasing distance from any of the tracked markers

3.3   Patient images
Figure 9 shows a projection image from the CBCT scan of a pancreas cancer patient. The implanted gold seeds are visible close to the centre of the image. The patient also has a stent which is visible in the projection image, although the stent position was not used for the motion compensation.
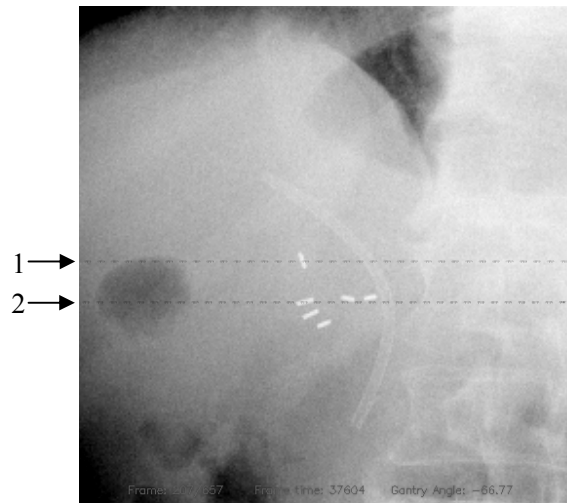
Figure 9: Projection image from CBCT scan of pancreas cancer patient. The longitudinal positions of the two slices shown in figure are indicated.

Figure 10 shows slices from the pancreas patient CBCT image with and without motion compensation. Images without motion compensation are shown on the left. Two transaxial slices are shown, the first at the level of the most superior seed (indicated as slice 1 in figure 9), and the second at the level of three other seeds (indicated as slice 2 in figure 9). Clear streak artefacts emanating from the seeds are visible in both of the transaxial slices without motion compensation. The image of the stent is also significantly blurred in the images shown in figure 10a, e and g. Streak artefacts from the seeds are much reduced in the motion compensated images and the stent boundary much sharper. However, the bony anatomy (e.g. spine) in the motion compensated images is observed to be less clear. Detail images of the region around the seeds and stent are shown in figure 11.

Figure 12 shows a projection image from the example breast patient image, illustrating the wire markers tracked as part of the motion correction procedure. Figure 13 shows two axial slices from the breast patient image before and after motion correction was applied. Streak artefacts were observed to be greatly reduced in the motion corrected image, both from the wire markers themselves and from nearby bony structures. Figure 14 shows details from the same images, where the artefact reduction can be seen more clearly. This reduction in streak artefacts made automatic contouring of the breast surface position more robust. The image quality of internal structures such as the ribs was also observed to be improved in the motion corrected image.
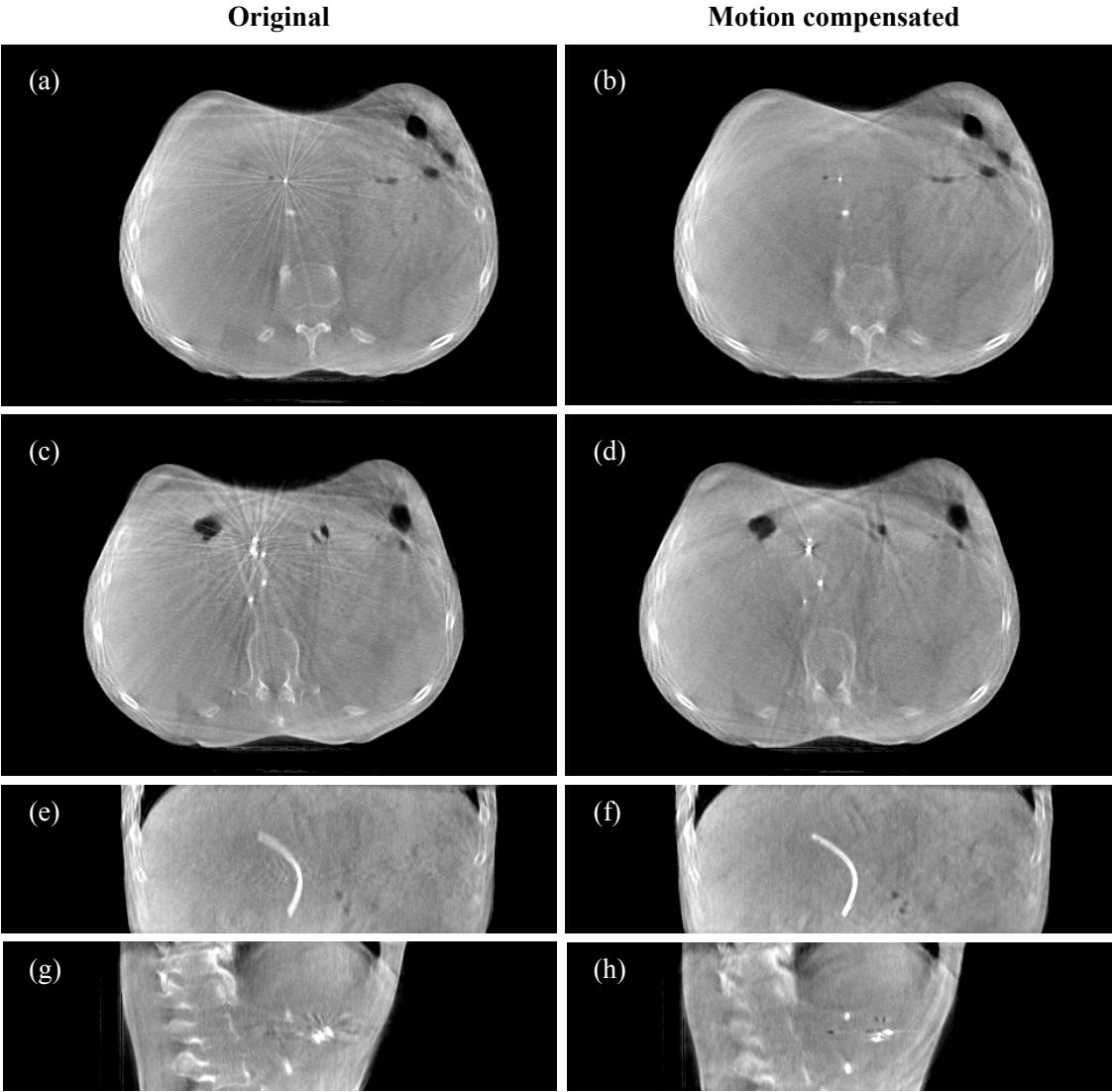
Original **Motion compensated**

Figure 10: Slices from pancreas patient CBCT image without motion compensation (left column) and with motion compensation (right column). (a & b) first transaxial slice, (c & d) second transaxial slice, (e & f) coronal slice, (g & h) sagittal slice.
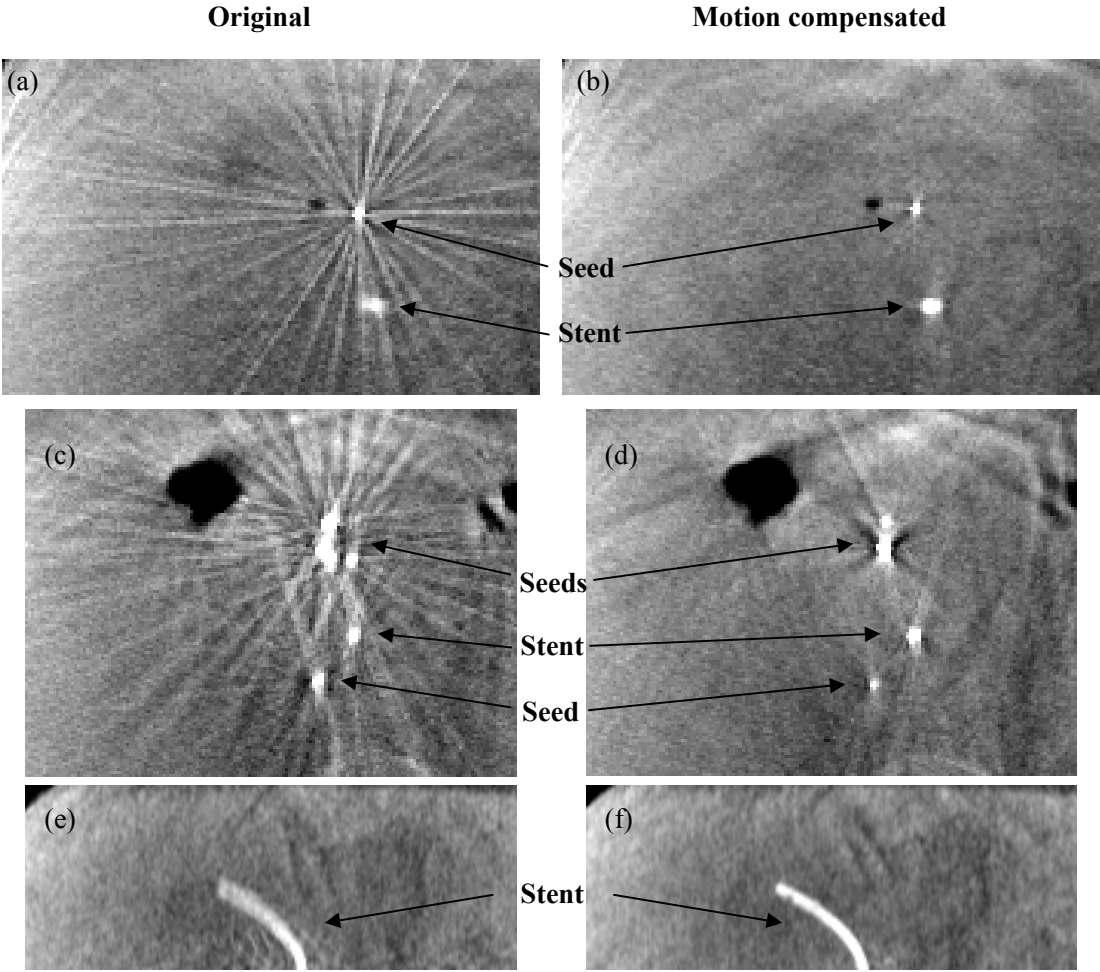
Original　　　　　　　　　　　**Motion compensated**

Figure 11: Detail from original (left column) and motion compensated (right column) patient images showing close up of region around seeds and stent. (a & b) first transaxial slice, (c & d) second transaxial slice, (e & f) coronal slice.
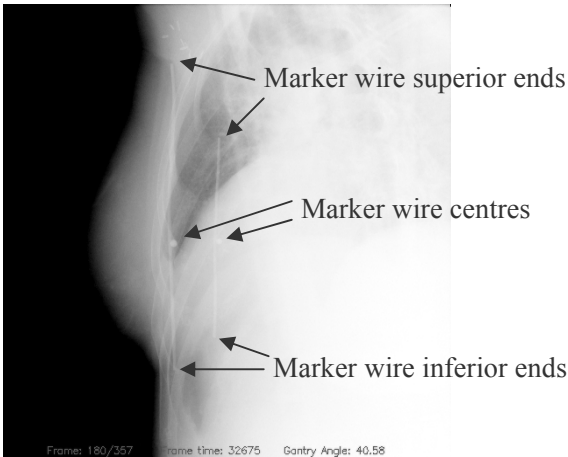
Figure 12: Projection image from breast patient CBCT acquisition showing marker wires on surface of patient.
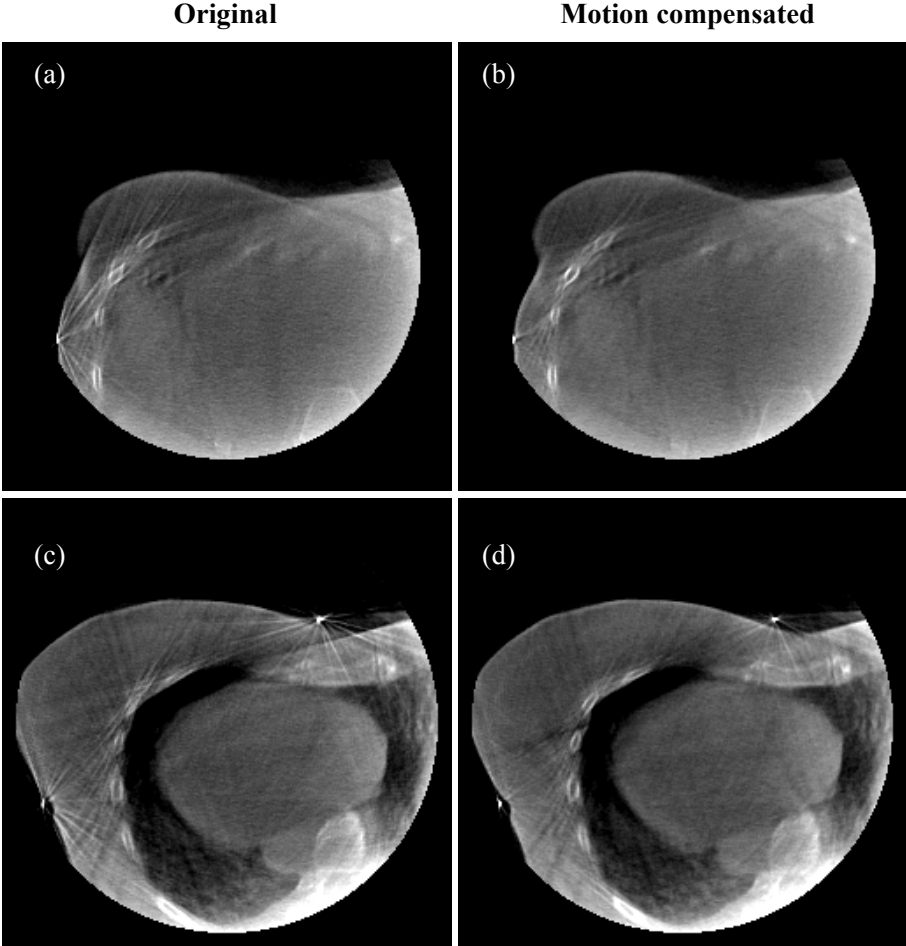
Original   **Motion compensated**

Figure 13: Original (a & c) and motion corrected (b & d) slices from breast patient CBCT reconstruction.
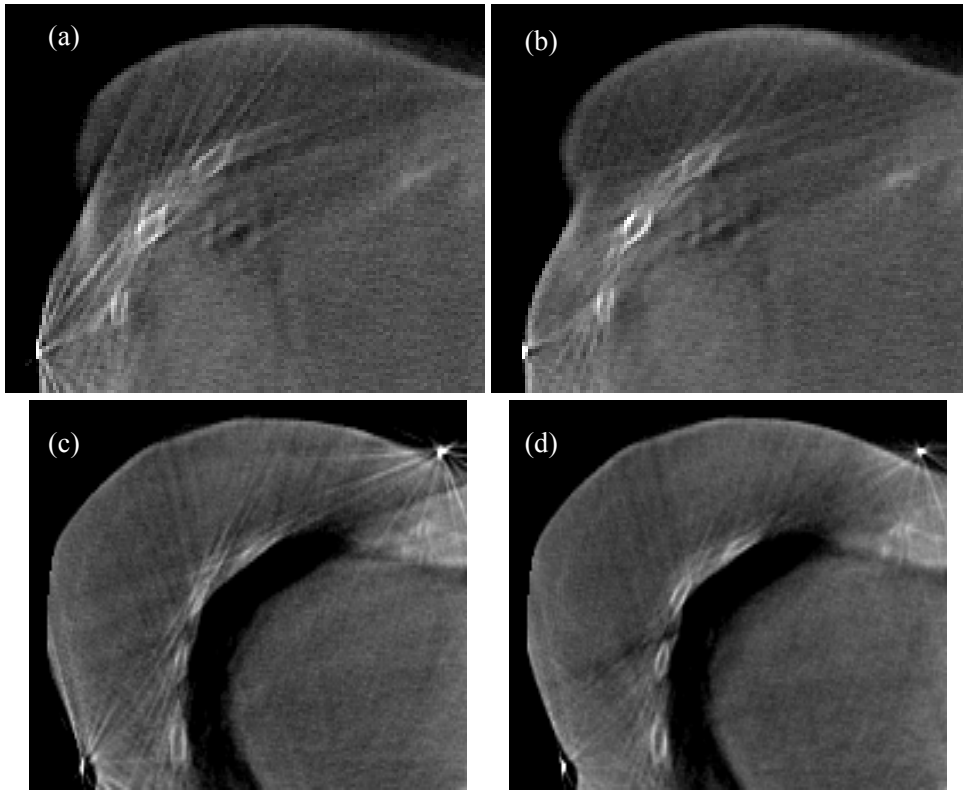
Figure 14: Detail from images shown in Figure 13. (a & c) Original image slices. (b & d) Motion corrected image slices.

4   Discussion

The reported method is intended to provide local motion blur and artefact correction that is effective for a specific region of interest so that anatomical structures can be better delineated for image guided therapy. Such structures exist at depth throughout the body, and as appendages to the body surface. The primary advantage of the motion correction method proposed in this paper is that all motion information is derived from the CBCT projection images themselves, with no requirement for prior imaging or motion models. However, the motion correction is achieved at a cost of possibly increased artefacts in areas far from the region of interest.

The breast phantom images presented in section 3.1 show that the 3D surface of a phantom can be re-produced to accuracy of the order of 1mm after tracking only a small number of markers placed on the surface. Although a rigid phantom was used, a tilting motion was applied, rather than a simple translation. Hence, a correction based on simple shifting of the projection images, as proposed in [12], does not perform as well (data not shown).

The virtual phantom tests demonstrate that the proposed motion correction method is also effective in the case of non rigid motion. In the first simulated experiment the tumour object's mean shape was accurately reproduced despite significant deformation being applied over the motion cycle. This is because the tracked markers acted as a reliable surrogate for the motion of the tumour edges. The virtual phantom tests also demonstrated two different scenarios in which the motion correction method may be useful: reconstruction of an object moving internally within the body, and reconstruction of body surface position.

In the patient images, motion artefacts, such as blurring and streaking emanating from the markers themselves was greatly reduced by the motion compensation method. In addition the markers themselves are reconstructed at the mean position of their 3D motion trajectory. The image of the stent in the pancreas patient image was also much sharper after application of the motion compensation algorithm. Since the position of the stent itself was not used for the motion compensation, this demonstrates that the motion compensation is effective for other objects in the vicinity of the tracked marker(s). In the breast patient CBCT the image quality of the ribs and chest wall were observed to be improved after motion compensation, even though only surface markers were tracked. However, motion blurring of the diaphragm and lower lung tissue was not reduced. This is as expected, since the motion of the ribs and chest wall is reasonably similar to that of the surface, whereas the diaphragm moves with larger amplitude.

As expected, motion correction on a local scale introduces artefacts in regions distant from the tracked markers, for example blurring of the spine in Figure 10. This is because the tracked seeds are moving relative to the spine, which is essentially static. Projection images from directions where the tracked seeds are superimposed onto the spine will be warped to place the seeds at their mean positions. This will introduce an error into the projected spine position, causing blurring in the reconstructed image. This illustrates the essential weakness of a 2D motion compensation technique: it cannot separate different objects projected onto the same pixel of a projection image. A possible solution to this problem may be to apply warping in 3D to the reconstructed volume, based on the fiducial marker positions detected in each projection image. This would require estimation of the 3D position of each detected marker in each projection image, for example using the method described by Poulsen, et al. [27]. The resulting motion correction method would be similar to that described by Li et al. [10], although using a 3D warp function derived from observed marker positions in the CBCT projections themselves rather than from a prior motion model.

The motion compensation method presented here is somewhat similar to the method of Hansis et al. [15], although we use a sparse set of radio-opaque markers as the tracked objects rather than contrast enhanced coronary arteries. Also, our method does not require a prior gated reconstruction to define the ideal artery positions, rather the mean marker positions are determined from the CBCT data itself.

There are also similarities with the motion correction method of Lu and Mackie [11], although here we apply the correction to wide-angle CBCT rather than fan-beam CT. This means that markers are tracked in 2D projection images rather than 1D CT profiles. In this manner out-of-plane motion can be tracked, as well as in-plane motion, which is likely to be significant for respiratory motion. Marker tracking in cone beam projections is also more robust, for example by continuing to track markers which move longitudinally between slices. In addition the method presented here does not rely on a simplistic patient motion model to allow an approximate global correction. Rather, it is accepted that motion will only be fully corrected in the vicinity of the tracked markers, which are located in regions of specific clinical interest. This pragmatic approach is more likely to be applicable in real-world situations and we have demonstrated it with real phantom and clinical images as well as simulated data.

In this study we used manual tracking of implanted markers. Automatic tracking of the markers, using methods such as that of Tang et al. [28], would be a feasible extension to speed up the process. A further desirable extension would be to use natural markers within the body to avoid the need for implantation of seeds. However, it is challenging to find natural markers which are sufficiently visible to be identified from an appropriate number of projection angles.

5   Conclusion

A motion compensation method for CBCT based on warping of projection images has been developed and tested. Radio-opaque markers within or on the surface of the patient are tracked and their mean 3D position is calculated. The projection images are then warped before reconstruction to place each marker at the forward projection of its mean position. The method has been shown to greatly reduce motion artefacts in CBCT images of a moving breast phantom, allowing the true surface shape to be accurately recovered. Simulated images of a virtual phantom demonstrated good performance of the motion correction method for non-rigid motion. Clinical CBCT images of a pancreas and a breast radiotherapy patient showed improved image quality in the locality of the radiotherapy target.

References

1.   McBain CA, Henry AM, Sykes J, Amer A, Marchant T, Moore CJ, et al. X-ray volumetric imaging in image-guided radiotherapy: The new standard in on-treatment imaging. Int. J. Radiat. Oncol. Biol. Phys. 2006;64(2):625.

2.   Smitsmans MH, de Bois J, Sonke JJ, Betgen A, Zijp LJ, Jaffray DA, et al. Automatic prostate localization on cone-beam CT scans for high precision image-guided radiotherapy. Int. J. Radiat. Oncol. Biol. Phys. 2005;63(4):975-84.

3.   Hawkins MA, Brock KK, Eccles C, Moseley D, Jaffray D, Dawson LA. Assessment of residual error in liver position using kV cone-beam computed tomography for liver cancer high-precision radiation therapy. Int. J. Radiat. Oncol. Biol. Phys. 2006;66(2):610-619.

4.   Sonke JJ, Zijp L, Remeijer P, van Herk M. Respiratory correlated cone beam CT. Med. Phys. 2005;32(4):1176-86.

5.   Li T, Xing L, Munro P, McGuinness C, Chao M, Yang Y, et al. Four-dimensional cone-beam computed tomography using an on-board imager. Med. Phys. 2006;33(10):3825-3833.

6.   Dietrich L, Jetter S, Tucking T, Nill S, Oelfke U. Linac-integrated 4D cone beam CT: first experimental results. Phys. Med. Biol. 2006;51(11):2939-2952.

7.   Rit S, Wolthaus JWH, van Herk M, Sonke J-J. On-the-fly motion-compensated cone-beam CT using an a priori model of the respiratory motion. Med. Phys. 2009;36(6):2283-2296.

8.   Rit S, Sarrut D, Desbat L. Comparison of Analytic and Algebraic Methods for Motion-Compensated Cone-Beam CT Reconstruction of the Thorax. Medical Imaging, IEEE Transactions on 2009;28(10):1513-1525.

9.   Schäfer D, Borgert J, Rasche V, Grass M. Motion-compensated and gated cone beam filtered back-projection for 3-D rotational X-ray angiography. IEEE Trans. Med. Imaging 2006;25(7):898-906.

10.   Li T, Schreibmann E, Yang Y, Xing L. Motion correction for improved target localization with on-board cone-beam computed tomography. Phys. Med. Biol. 2006;51(2):253-267.

11.   Lu W, Mackie TR. Tomographic motion detection and correction directly in sinogram space. Phys. Med. Biol. 2002;47(8):1267-1284.

12.   Ali I, Ahmad S. SU-GG-I-17: A Technique for Removing Motion Related Image Artifacts in KV Cone-Beam CT From On-Board Imager: 4D-CBCT Implications

(Abstract from 50th AAPM Annual Meeting, Houston, July 2008). Med. Phys. 2008;35(8):2646.

13. Perrenot B, Vaillant R, Prost R, Finet G, Douek P, Peyrin F. Motion Correction for Coronary Stent Reconstruction From Rotational X-ray Projection Sequences. IEEE Trans. Med. Imaging 2007;26(10):1412-1423.

14. Schäfer D, Movassaghi B, Grass M, Schoonenberg G, Florent R, Wink O, et al. Three-dimensional reconstruction of coronary stents in vivo based on motion compensated X-ray angiography. In: Medical Imaging 2007: Visualization and Image-Guided Procedures; 2007; San Diego, CA, USA: SPIE; 2007.

15. Hansis E, Schäfer D, Dössel O, Grass M. Projection-based motion compensation for gated coronary artery reconstruction from rotational x-ray angiograms. Phys. Med. Biol. 2008;53(14):3807-3820.

16. Marchant TE, Amer AM, Moore CJ. Measurement of inter and intra fraction organ motion in radiotherapy using cone beam CT projection images. Phys. Med. Biol. 2008;53(4):1087-1098.

17. Evans PM. Anatomical imaging for radiotherapy. Phys. Med. Biol. 2008;53(12):R151-R191.

18. Kothary N, Dieterich S, Louie JD, Chang DT, Hofmann LV, Sze DY. Percutaneous Implantation of Fiducial Markers for Imaging-Guided Radiation Therapy. American Journal of Roentgenology 2009;192(4):1090-1096.

19. Barrodale I, Skea D, Berkley M, Kuwahara R, Poeckert R. Warping digital images using thin plate splines. Pattern Recognition 1993;26(2):375-376.

20. Feldkamp LA, Davis LC, Kress JW. Practical cone-beam algorithm. J. Opt. Soc. Am. A 1984;1(6):612-619.

21. Kinoshita R, Shimizu S, Taguchi H, Katoh N, Fujino M, Onimaru R, et al. Three-Dimensional Intrafractional Motion of Breast During Tangential Breast Irradiation Monitored With High-Sampling Frequency Using a Real-Time Tumor-Tracking Radiotherapy System. Int. J. Radiat. Oncol. Biol. Phys. 2008;70(3):931-934.

22. Besl PJ, McKay HD. A method for registration of 3-D shapes. Pattern Analysis and Machine Intelligence, IEEE Transactions on 1992;14(2):239-256.

23. Muller-Merbach J. Simulation of x-ray projections for experimental 3d tomography. Technical report, Image Processing Laboratory Department of Electrical Engineering Linkoping University, SE-581 83, Sweden. 1996.

24. Henry AM, Ryder WDJ, Moore C, Sherlock DJ, Geh JI, Dunn P, et al. Chemoradiotherapy for Locally Advanced Pancreatic Cancer: a Radiotherapy Dose Escalation and Organ Motion Study. Clin. Oncol. 2008;20(7):541-547.

25. Schellenberg D, Goodman KA, Lee F, Chang S, Kuo T, Ford JM, et al. Gemcitabine Chemotherapy and Single-Fraction Stereotactic Body Radiotherapy for Locally Advanced Pancreatic Cancer. Int. J. Radiat. Oncol. Biol. Phys. 2008;72(3):678-686.

26. Koong AC, Le QT, Ho A, Fong B, Fisher G, Cho C, et al. Phase I study of stereotactic radiosurgery in patients with locally advanced pancreatic cancer. Int. J. Radiat. Oncol. Biol. Phys. 2004;58(4):1017-1021.

27. Poulsen PR, Cho B, Keall PJ. A Method to Estimate Mean Position, Motion Magnitude, Motion Correlation, and Trajectory of a Tumor From Cone-Beam CT Projections for Image-Guided Radiotherapy. Int. J. Radiat. Oncol. Biol. Phys. 2008;72(5):1587-1596.

28. Tang X, Sharp GC, Jiang SB. Fluoroscopic tracking of multiple implanted fiducial markers using multiple object tracking. Phys. Med. Biol. 2007;52(14):4081-4098.